Characterization of the Fe-6.5wt%Si Strip with Rapid Cooling Coupling Deep Supercooled Solidification

Bo Wang, Guangxun Li, Yang Wang, Yingtao Su, Huilan Sun, Zhihong Guo, Di Zhang,* and Zhongqi Dong*

ACCESS | Metrics & More | Article Recommendations

ABSTRACT: The phase transition law between ordered and disordered phases, second phase reinforcement, microstructure, and mechanical properties were systematically studied in the rapid cooling coupling deep supercooled solidification process through an arc melting furnace, electromagnetic induction heating, and high-speed cooling single-roll technology. The results show that uniform nucleation and grain refinement are promoted under rapid cooling coupling deep supercooled solidification, and the phase transition from the disordered phase (A2) to the ordered phase (B2 and DO_3) is also effectively suppressed. The decreased crystalline grain size and optimized microstructure morphology improved the plasticity and magnetic property. The Fe-6.5wt%Si steel strip at 42 m/s has a good phase composition of Fe (predominant), Fe_2Si, and SiC. The sample showed an equiaxed ferrite crystal structure, and the saturation magnetizations were 302.5 and 356.6 emu/g in the parallel magnetic direction and the vertical magnetic direction, respectively. This phase transition behavior contributed to the exceptional magnetic property of the Fe-6.5wt%Si steel.
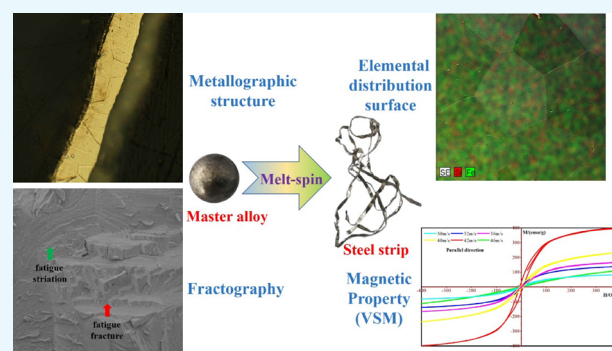
1. INTRODUCTION

Fe-6.5wt%Si high-silicon steel has become a popular soft magnetic material[1,2] for the manufacture of generators, frequency motors,[3] high-frequency transformers,[4] choke coils and high-frequency magnetic shieldings,[5] and other electrodynamic instruments in the electricity and telecommunications field,[6−8] which are attributed to its high electrical resistivity and good saturation magnetization. It has the potential to reduce noise during the working process of the motor, mainly attributing to the excellent soft magnetic properties, such as the low iron loss, high magnetic conductivity, and low magnetostriction coefficient.[9,10] Even so, the iron loss still could cause enormous electricity consumption every year, which accounts for 2.5−4.5% of the annual global generating capacity. Therefore, further increasing magnetic induction and decreasing iron loss have become an imperative requirement. Meanwhile, a high silicon content could also increase the aging phenomenon, enhance the brittleness, and significantly decrease the plasticity.[11,12] High-silicon steel could result in cracks during the rolling process and often requires multiple rolling heat treatment processes. The high-silicon steel produced in the conventional process has a high cost. So, the preparation of high-silicon steel materials with excellent performance in the rapid cooling process is a place worthy of in-depth study. Thus, a rapid cooling coupling deep super-cooled solidification process of Fe-6.5wt%Si has been proposed and discussed in this paper.

Crystal grain size is the main factor affecting the iron loss,[13−15] and fine grains are more favorable for inhibiting the high-frequency iron loss because increasing the grain size could not only decrease the hysteresis loss (dominance in low frequency) but also increase the eddy-current loss (dominance in high frequency). Meanwhile, decreasing the density of the antiphase domain boundaries could reduce the hysteresis loss and iron loss.[16,17] During the ordered phase precipitation process, the antiphase domain boundary on magnetic domain walls could reduce the magnetic conductivity, improve the coercivity, and then deteriorate the magnetic energy significantly. A large number of studies presented that controlling the silicon content,[18] doping inhibitor elements,[10,19] and optimizing the cooling system[20] could improve the crystal grain size and the transformation process of the ordered phase and then improve the plasticity and machining
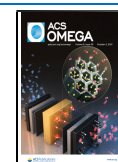
property. Increasing the silicon content could improve the grain boundary migration, resulting in the large-size crystal grain formation, which then significantly deteriorates the plasticity of the Fe−Si steel. Grain boundary polarized elements (e.g., Cu, Sn, Cr, Mo, Nb, and Bi)[5,7,11] and dispersed second phase formation (e.g., MnS, MnSe, AlN, and NbC)[14,16,18] also could restrain the primary recrystallization grain growth and pin the grain boundaries. The grain boundaries will migrate rapidly, engulf the surrounding fine grains, and grow abnormally when the annealing temperature reaches the decomposition temperature of the inhibitor. Meanwhile, increasing the grain boundary proportion could increase the grain boundary strength (especially in the Σ3 and Σ9 boundary),[21] restrain the crack growth, and then improve the plasticity and machining property. However, it is difficult for the conventional process to improve the Σ3 and Σ9 boundary proportion. The nonequilibrium quenching-rapid solidification processes, which mainly focus on the rapid cooling to change the phase precipitation path, such as rapid solidification and injection molding, are used to avoid or eliminate the ordered phase formation.[22]

The rapid cooling process and deep supercooled solidification technology could also promote the solidification process of liquid metals. Deep undercooling and rapid cooling make the alloy melt and have a large initial nucleation undercooling degree,[23] thereby promoting nucleation. Rapid solidification is conducive to grain refinement and promotes homogeneous nucleation.[24] This paper addresses the effect of ultrahigh-speed cooling (30−50 m/s) on the ribbon formation and alloy solidification processes of the Fe-6.5wt%Si strip and explores the mechanical and magnetic properties of the high-silicon steel strip. The phase transition process, microstructure, fractography, magnetic property, and Vickers hardness of the samples were also confirmed and observed.

2. EXPERIMENTAL SECTION

The raw materials used in the study were iron (mass percent of 99.9%) and silicon (mass percent of 99.9%). The Fe−Si parent alloy was prepared in an arc melting furnace, and the mass ratio of Fe to Si is 93.5:6.5. First, an electronic balance with an accuracy of one in ten thousand is used to weigh the alloy raw materials with an iron and silicon ratio of 93.5:6.5. The uniform mixture materials were then placed in a copper crucible of the arc melting furnace, controlling the vacuum of the smelting chamber at 2.0×10^{-3} Pa and the gas pressure at −0.07 to −0.10 MPa with high-purity Ar (99.999%). The alloy particles were melted in the copper crucible of the arc smelting furnace, and the alloy ingots were repeatedly smelted for 6−8 times to make the alloys evenly mixed.

After that, the Fe−Si master alloy was smelted again in the single-roll equipment with a high-energy electromagnetic heating device for the purpose of rapid cooling coupling deep supercooled solidification. During the solidification of the alloy, the vacuum chamber for smelting was controlled at 6.0×10^{-4} Pa, and the gas pressure with high-purity Ar was at −0.07 to −0.05 MPa. The parent alloy was placed in a quartz tube and heated by electromagnetic induction until melting. After the alloy was heated enough to melt fully, high-purity Ar was injected into the hollow quartz tube under the pressure of the gas storage tank. The molten Fe−Si alloy was sprayed through a nozzle at the bottom of the quartz tube onto the surface of the rapidly rotating copper rod and rapidly solidified. Under the action of centrifugal force on the surface of the copper rod,

the molten Fe−Si alloy formed thin strips of high-silicon steel at various cooling rates.

The mineral composition of the Fe−Si sample was determined by X-ray diffraction (XRD, Rigaku D/MAX-2500). The microstructure analysis was carried out by scanning electron microscopy (SEM, Bruker TESCAN Vega3) fitted with an energy-dispersive spectrometer (EDS, X-Flash 410M). The thermal evolution of the Fe−Si steel strip sample was carried out by thermogravimetry (TG) and differential thermal analysis (DTA) (Linseis, DTA, PT1600) equipment from room temperature to 1400 °C at a heating rate of 5 °C·min^{-1} with the vacuum atmosphere at 8 mbar. The magnetic property of the steel strip sample was obtained by vibrating sample magnetometer (VSM, Quantum Design, VersaLab) equipment at room temperature. The Vickers hardness was confirmed by HVS-30 equipment.

3. RESULTS AND DISCUSSION

3.1. Effect of High Wheel Speed on the Morphology of the Sample.
The cooling rate decreases monotonously as the wheel speed decreases, and the ductility of the sample increases. The morphology of the sample is shown in Figure 1.
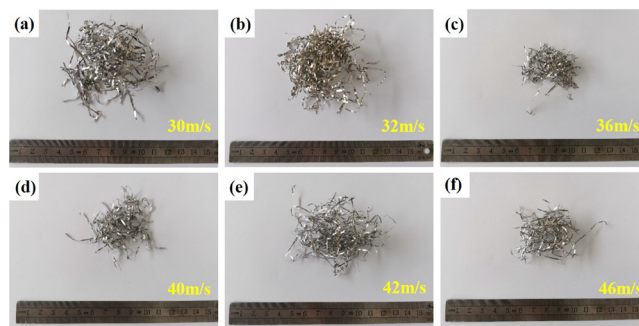

Figure 1. Photos of the Fe-6.5wt%Si steel strip using different wheel speeds: (a) 30, (b) 32, (c) 36, (d) 40, (e) 42, and (f) 46 m/s.

There is no significant difference in the morphology of the sample from 30 to 46 m/s, but the thickness and width of the sample decrease significantly with the increase in wheel speed. The decrease in the thickness and width of the sample makes it more difficult to detect the sample. The changes in sample thickness and width are shown in Table 1. The average thickness and width of the sample with a wheel speed of 46 m/s reach 5.9 μm and 9.8 dmm.

At the same time, the surface of the sample with a roller surface is smoother than the free surface, which is mainly due to the different solidification environment and conditions on both sides of the sample. During belt casting, the molten alloy is subjected to high-pressure gas flowing through the nozzle to contact the cooling copper roller and is subjected to cooling and restraint of the cooling copper roller, so the surface formed is relatively flat. As the free surface is far away from the surface of the copper roller, it is not constrained by the copper roller during solidification, and the cooling rate is relatively small compared with the surface of the roller; also, because of the mechanical vibration of the equipment and the impact of the external high-speed air flow, macro fluctuations are formed on the surface.

3.2. Phase Formation and Transition Process.
The dynamic and thermodynamic processes of nucleation generation, crystal growth, and crystal structure transformation

Table 1. Thickness and Width of the Melt-Spun Ribbons Prepared Using Different Wheel Speeds

wheel speed (m/s)	30	32	36	40	42	46
thickness (μm)	21.6 (±1.5)	16.5 (±1.2)	13.0 (±1.4)	10.2 (±1.0)	8.6 (±0.8)	5.9 (±0.7)
width (dmm)	18.1 (±0.6)	16.5 (±0.4)	13.9 (±0.5)	12.6 (±0.3)	11.3 (±0.4)	9.8 (±0.2)

always depend on the degree of undercooling and temperature gradient significantly. Meanwhile, deep supercooled rapid solidification (rpm from 30 to 50 m/s) also has a great effect on the process of mineral formation/transition and the stability of the crystal structure,[25] as shown in Figure 2. The space group and lattice parameters of the cell at different rotating speeds correspond to the standard phase.
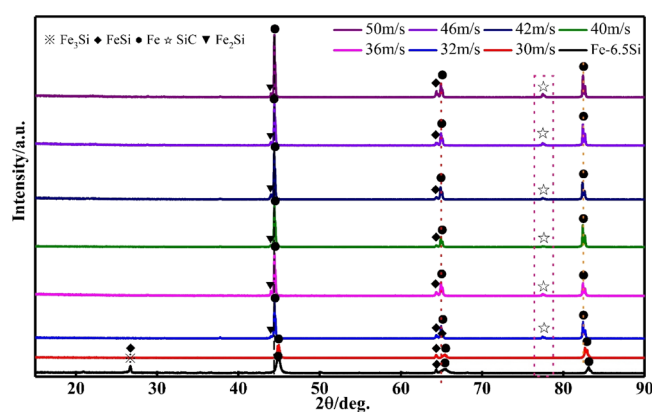

Figure 2. XRD patterns of the Fe-6.5wt%Si steel strip with rpm from 30 to 50 m/s.

Figure 2 shows the XRD pattern of the steel strip from the master alloy to the rapidly solidified thin strip. The XRD curve of the master alloy shows the presence of FeSi and Fe_3Si. FeSi and Fe_3Si are important components of ordered phases B2 and DO_3, respectively. Among them, Fe_3Si belongs to the cubic structure and the $Im\bar{3}m$ (229) space group. The lattice parameter $a = b = c$ is 2.84 Å, the cell angle $\alpha = \beta = \gamma$ is 90°, and the cell volume is 22.99 Å^3. When the speed increased to 30 m/s, the cubic phase Fe_3Si disappeared. The strip steel from 30 to 50 m/s has a phase composition similar to FeSi. The results show that the ordered phase DO_3 is basically suppressed, and the ordered phase B2 is partially suppressed.

As shown in Figure 3, it can be seen that in the disordered A2 phase, Fe and Si are distributed randomly. The ordering in
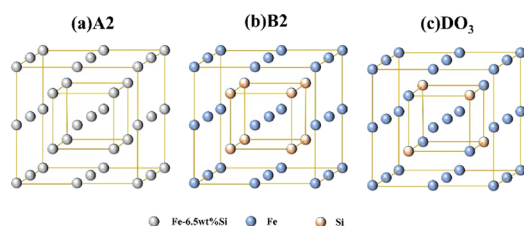
Figure 3. Crystal structures of Fe-6.5wt%Si for (a) A2, (b) B2, and (c) DO_3 phases. Blue and orange atoms are Fe and Si, respectively.

Fe-6.5wt%Si occurs by the pairing of Fe and Si atoms. The nearest neighbor pairing results in B2 ordering, and the next-nearest neighbor pairing results in DO_3 ordering. The B2 ordering occurs when one silicon atom tends to occupy one of the eight BCC sites, and the DO_3 ordering occurs when two silicon atoms tend to occupy two adjacent BCC sites.[26]

Compared with the sample at 30 m/s, the diffraction angle (2θ) decreases slightly (44.89 → 44.44°, 65.40 → 64.96°, and 82.71 → 82.47°) with increasing of the rpm, indicating that the interplanar spacing of Fe increases, which is calculated by the Bragg equation ($2d \sin \theta = n\lambda$). Meanwhile, a small amount of SiC also could be detected, while the carbon element may have come from the iron powder or the additional impurities in the arc melting furnace. The Fe crystal belongs to the cubic structure and $Im\bar{3}m$ (229) space group, while the crystal orientations are (110), (200), and (211). The Fe atom distributes in all the eight corners and the center position, while the Si atom coexisting with partial Fe atoms only distribute in the diagonal positions with the crystal orientation in $[111]$. The FeSi crystal belongs to the hexagonal structure and $P\bar{3}m1$ (164) space group, while the crystal orientations are (102), (022), and (300).

The interplanar spacing and cell volume, corresponding to the strongest diffraction peaks and the unit cell parameters of Fe and FeSi, were also calculated in the steel strip for different rpm values, as shown in Figure 4. The atomic vibration/substitution process and the self-adjustment of the crystal structure have lots of effects on the mineral formation and transformation processes, which improve the mechanical property, the magnetic property, and the chemical stability. Figure 4a,b shows that increasing the rpm (or the subcooling) would increase the cell volume, the lattice parameters (a, b, and c), and the interplanar spacing of Fe gradually when the rpm is lower than 42 m/s. Nevertheless, with increasing the subcooling higher than 42 m/s, the crystal parameters would show an opposite tendency. Meanwhile, the lattice parameter $a = b$ and the cell volume increase first before the rpm at 42 m/s and then decrease gradually, while the lattice parameter c also shows an opposite tendency. The interplanar spacing of (102) decreases first until 42 m/s and then increases gradually, while the interplanar spacings of (022) and (030) increase slightly first and then decrease sharply. In conclusion, increasing supercooling (the rpm higher than 32 m/s) could restrain the transition process from the disordered phase Fe to the ordered phases FeSi and Fe_3Si and improve the cell volume and the interplanar spacing (exclusion of (102) of FeSi).[27]

The TG-DSC curves of the Fe-6.5wt%Si arc melting sample and steel strip sample varying with the selected rpm (42 m/s) in the nonisothermal heating process are illustrated, as shown in Figure 5. The phase transition behavior and thermal stability of the thin strip were analyzed with thermogravimetric and differential scanning calorimetry (TG-DSC).

As shown in Figure 5, the DSC curve presents two obvious characteristics, namely, the orderly transition from the disordered A2 to the orderly B2+DO_3 phase and the order−disorder transition. The thin strip prepared by rapid cooling and deep subcooling is disordered in the initial stage of heating. By heating the material to the B2+DO_3 phase region, an exothermic reaction occurs at 550−580 °C. At this temperature, the peak on the DSC curve can be attributed to the transition from A2 to the ordered phase of B2+DO_3 and may also be accompanied by part of the transition from DO_3 to B2. The second exothermic transition of the DSC curve occurs
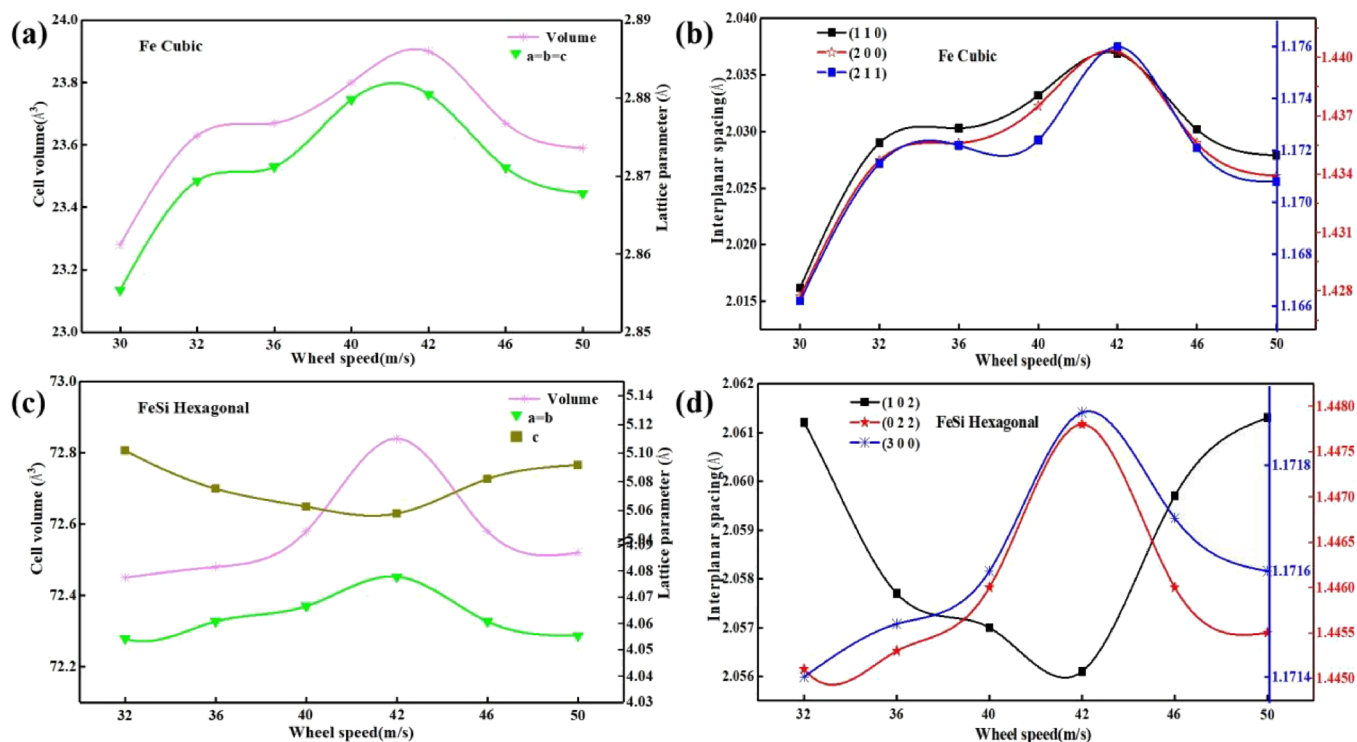
Figure 4. Crystal parameter of the Fe-6.5wt%Si steel strip: (a) cell volume and lattice of Fe, (b) interplanar spacing of Fe, (c) cell volume and lattice of FeSi, and (d) interplanar spacing of FeSi.
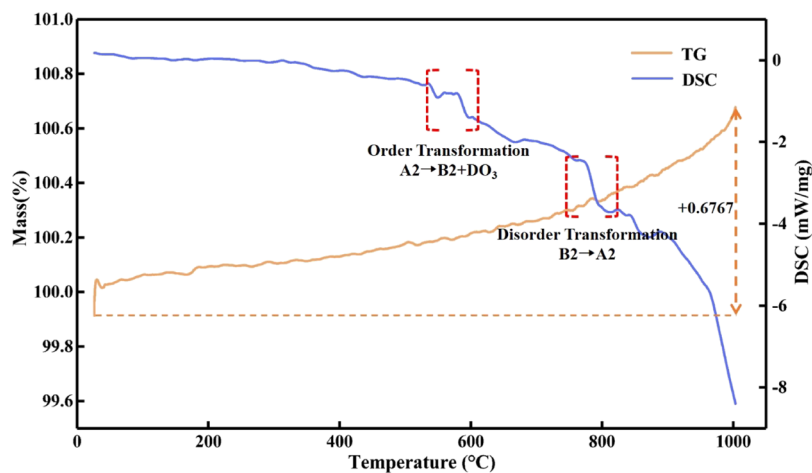

Figure 5. TG-DSC of the Fe-6.5wt%Si steel strip at 42 m/s.

when the material is heated to 750−785 °C.[28] The second exothermic transition should be attributed to the transition from the ordered phase (B2) to the disordered phase (A2) of the material. The TG curve mainly shows that the material has a slight weight gain during the heating process. In general, the samples at a cooling rate of 42 m/s maintain good thermal stability.

3.3. Microstructure and Energy Spectrum Analysis. In the deep supercooled solidification process, the high-temperature-melting alloy would flow through the cuprum roll surface with a rapid cooling system, which is also forced to cool down quickly under the effect of a high-pressure Ar fluid and the constrained action of the roll surface. The critical nucleation radius decreases, while the ion migration rate decreases. Moreover, a great number of nucleation starts to form significantly under the large subcooling conditions. As shown

in the surface micrograph in Figure 6, different wheel speeds and their associated cooling rates significantly affect the grain size of equiaxed grains on the pulley side of the strip. The average grain sizes of the Fe-6.5wt%Si thin strip are 28.5, 20.6, and 8 μm at cooling rates of 20, 30, and 40 m/s, and they all show regular central equiaxed grains.
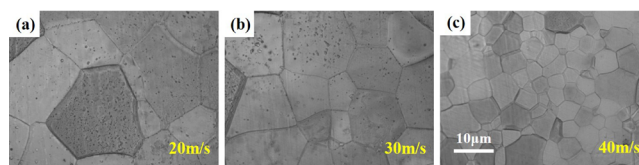

Figure 6. Wheel side surface micrographs of the Fe-6.5wt%Si steel strip at different speeds: (a) 20, (b) 30, and (c) 40 m/s.

The high-speed single-roll casting strip and solidification could also promote the formation process of regular central equiaxed grains with the straight crystal boundary, as shown in Figure 6. The Fe-6.5wt%Si steel strip with 42 m/s has a regularly pentagonal grain distribution with sizes ranging from 5 to 10 μm. Furthermore, lots of precipitates and inclusions could also be observed, which mainly distribute close to the clear grain boundaries.

The metallographic structure, BSE images, EDS analysis, and fractography structure of the Fe-6.5wt%Si steel strip with 42 m/s are also confirmed, as shown in Figure 7, Figure 8, and
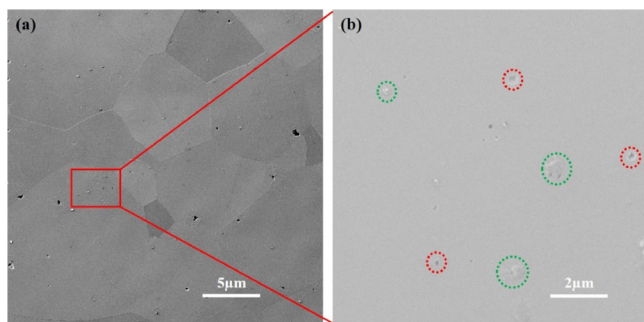

Figure 7. SEM images of the Fe-6.5wt%Si steel strip at 42 m/s: (a) microstructure and (b) precipitates and inclusions.

Table 2. The microstructure of the cast strip steel (Figure 8a) has no significant difference between the center and the edge. The homogeneous nucleation process and rapid crystal growth contribute to the equiaxed crystal formation, which should be

Table 2. EDS Results of the Fe-6.5wt%Si Steel Strip Corresponding to Figure 8b (Atom Percentage)

positions	Fe	Si	C	Fe/Si molar ratio
$\alpha_\dagger$	88.67	11.33		3.94:1
$\beta_\dagger$	92.58	7.42		6.27:1
$\gamma_\dagger$	49.00	6.28	44.72	3.92:1
$\delta_\dagger$	46.58	6.21	47.21	3.77:1

mainly attributed to the good heat transfer property and the large degree of supercooling by the high-speed single-roll process. The fracture mechanism and crack network of the steel strip are also confirmed according to the metallographic section of transverse cross sections in the rolling direction shown in Figure 8c. A visible boundary is observed within the fatigue striation (marked green) and the fatigue fracture surface (marked red). Further analysis shows that there is no obvious plastic deformation in the fractography structure, which should be mainly attributed to the fatigue failure process of equiaxial ferrite.

As shown in Figure 8b, the BSE image shows two main gray equiaxed grains: darker gray regions (similar to the $\alpha_\dagger$ grain) and light gray regions (similar to the $\beta_\dagger$ grain). The elemental distribution surface (Figure 8d−f) shows that all the Fe and Si elements distribute uniformly in the selected region, which indicates that the Fe-containing and the Si-containing phases have good consistency. The mineral composition and distribution are all confirmed by means of the atomic composition percentage (Table 2) of the characteristic region and the second-phase particle with the XRD results. As shown in Figure 9, it shows that the selected regions of $\alpha_\dagger$ and $\beta_\dagger$ only
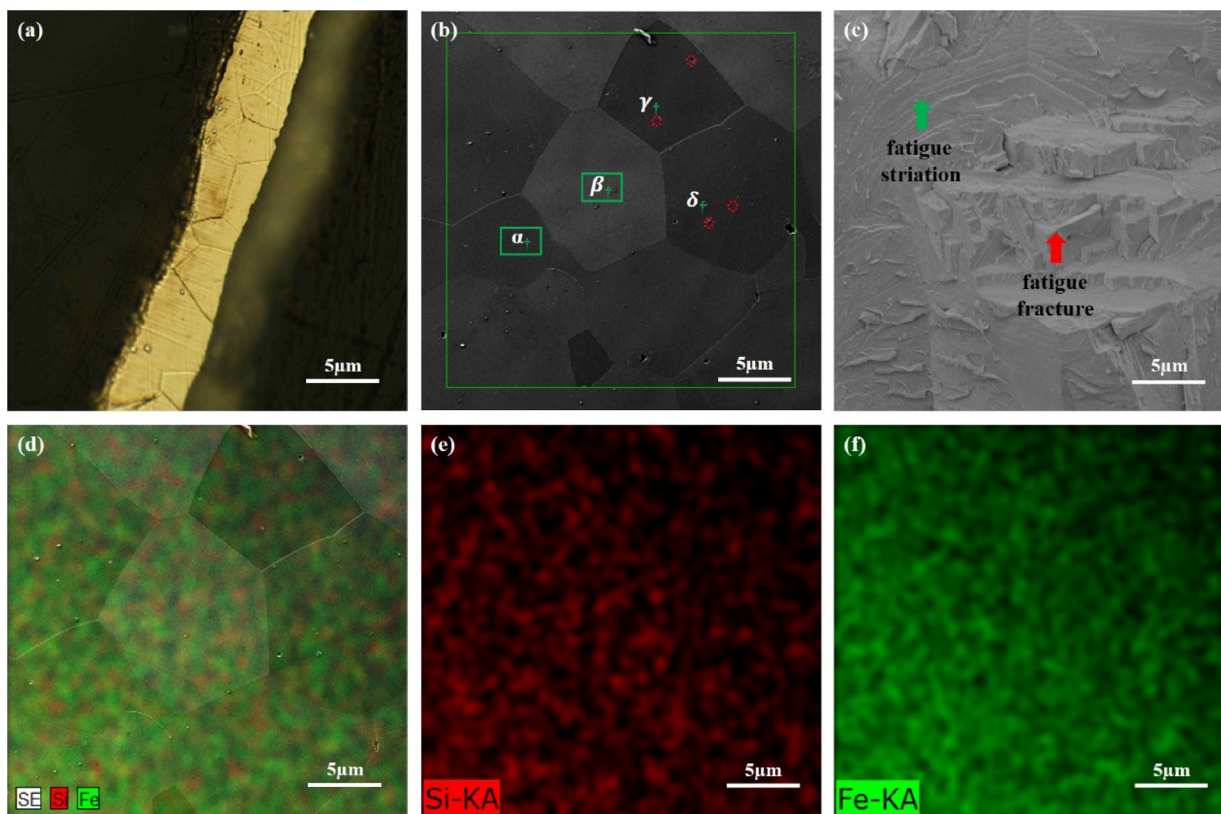

Figure 8. Microstructure and BSE images of the Fe-6.5wt%Si steel strip at 42 m/s: (a) metallographic structure, (b) BSE image, (c) fractography, (d) elemental distribution surface, (e) Si distribution, and (f) Fe distribution.
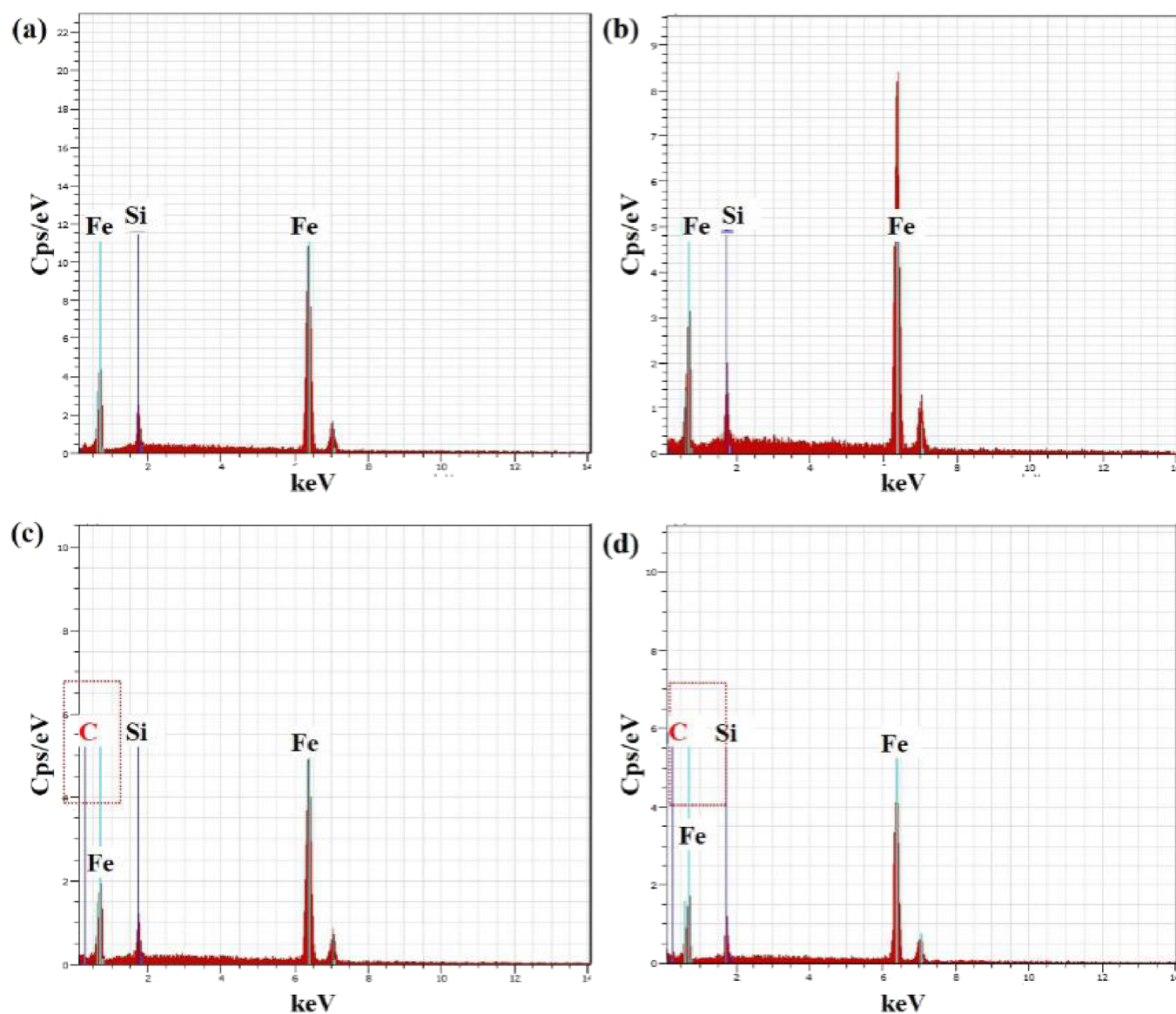
Figure 9. Energy dispersion spectrum of the selected positions: (a) α, (b) δ, (c) γ, and (d) δ.

have the energy-dispersive spectra of Fe and Si elements, while the second-phase particles of $\gamma_{\dagger}$ and $\delta_{\dagger}$ have the energy-dispersive spectra of Fe, Si, and C elements. Therefore, the great number of second-phase particles should be attributed to the SiC phase, which is consistent with the XRD analysis (Figure 2). The darker gray grains should be attributed to the coexisting phases of Fe, Fe_2Si, and SiC, while the light gray grains should be attributed to the iron-rich coexisting phases of Fe and Fe_2Si.

3.4. Magnetic and Mechanical Properties. The magnetic properties of the Fe-6.5wt%Si arc melting and steel strip samples with rpm values of 30−46 m/s are also determined by the vibrating sample magnetometer equipment. The hysteresis loops are shown in Figure 10a−f, which indicates that the arc melting and steel strip samples also belong to the typical soft ferromagnetic material.[25] The magnetic properties of saturation magnetization (Ms), saturation remanence (Mr), and coercive force (Hc) are calculated based on the data in Figure 10, as shown in Figure 11.

According to Figures 10a,b and 11, the Ms, Mr, and Hc of the arc melting sample are 189.5 emu/g, 8.5 emu/g, and 9.4 Oe parallel to the magnetic direction, and there is no obvious difference compared to the vertical magnetic direction. It indicates that the Fe-6.5wt%Si arc melting sample has good consistency, while the distribution and the growth direction of crystal grains have no obvious orientation.[24] When the magnetic properties of the steel strip samples were determined parallel to the external magnetic field (0 °C), Figure 11a shows that the Ms increased at first until 42 m/s and then decreased slightly. The Mr increases slightly from before 30 m/s compared with the arc melting sample and then decreases gradually until 46 m/s. The Hc decreases gradually before 40 m/s, and increasing the rpm from 40 to 46 m/s has no significant effect. The steel strip at 42 m/s has good magnetic properties, while the Ms, Mr, and Hc are 302.5 emu/g, 6.3 emu/g, and 8.6 Oe, respectively. When the magnetic properties of the steel strip samples were determined vertical to the external magnetic field (90 °C), Figure 11b shows that the magnetization behavior showed an obvious fluctuation. It should be mainly attributed to the crystal grain growth
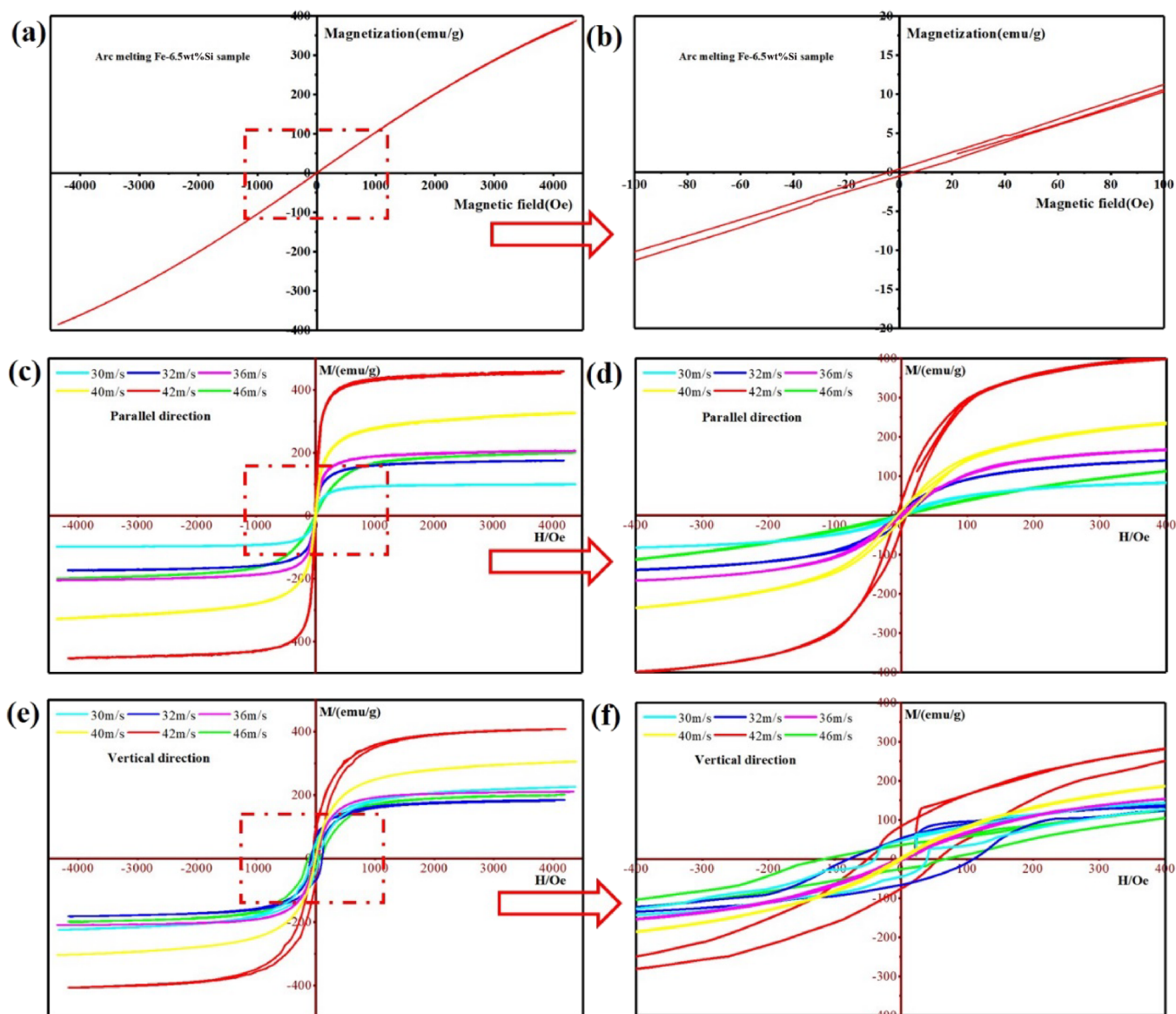
Figure 10. Hysteresis loops at room temperature of Fe-6.5wt%Si samples: (a,b) arc melting, (c,d) steel strip at the parallel direction, and (e,f) steel strip at the vertical direction.

orientation. The curve of Ms at the vertical direction also shows a similar vibration to the parallel direction, and the maximum Ms at 42 m/s is 356.6 emu/g. The Mr and Hc are 63.7 emu/g and 88.5 Oe. According to the crystal parameter (Figure 4) and the magnetic property (Figure 11), good crystallinity, large interplanar spacing, and fine grain distribution could also promote the electron motion and then improve the magnetic property. In the magnetization process, the fine grain size could decrease the width of the magnetic domain, improve the rotation of the magnetic domain, and then reduce the hysteresis loss. In conclusion, the steel strip at 42 m/s has the best Mr property and appropriate Ms and Hc properties.

Figure 12 shows that the Vickers hardness of the Fe-6.5wt% Si steel strip decreases gradually with increasing rpm from 23 to 50 m/s, while the Vickers hardness in the roller surface is always higher than the Vickers hardness in the free surface. It should be mainly attributed to the different supercooling and contact medium (roller and atmosphere), while the roller surface always has a larger supercooling. Increasing the rpm

could decrease the thickness of the steel strip, increase the cooling rate, and then reduce the difference of supercooling. Moreover, the free surface is far away from the cuprum roller, and the steel strip close to the free surface has no constraint during the solidification process. So, the Vickers hardness in the roller and free surfaces shows a significant difference, especially in the low rpm. As shown in Figure 6, the decrease in Vickers hardness of the Fe-6.5wt%Si thin strip is related to the decrease in grain size. The ordered phase is effectively suppressed with the increase in the cooling rate. The ductility of the sample was improved.[29] Therefore, the Vickers hardness of the Fe-6.5wt%Si thin strips gradually decreased. Meanwhile, when the rotating speed reaches 46 m/s, the Vickers hardness of the two surfaces gradually approaches each other and tends to be stable. The Vickers hardness values of the roller surface and the free surface at 42 m/s are 123.8 and 118.7 HV.

The ordered domain of B2 and DO_3 mainly formed during the orderly transformation process of the Fe-6.5wt%Si steel strip. This appears to match well with the so-called ductile-to-
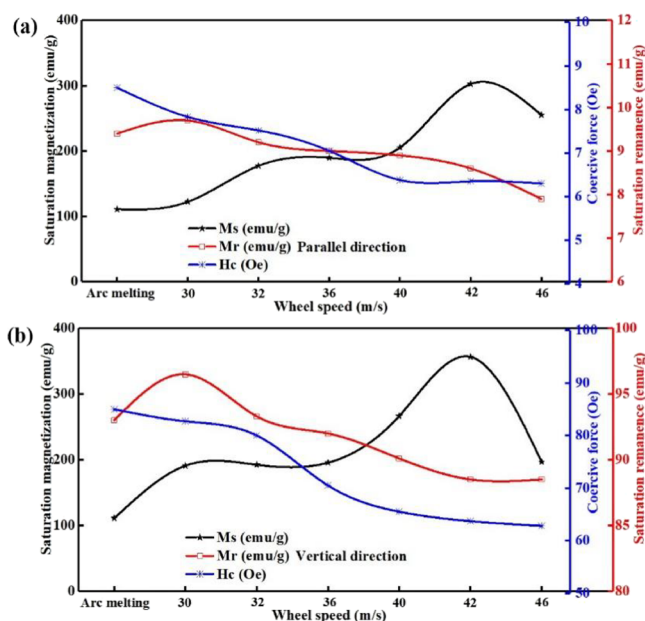
Figure 11. Magnetic properties of the sample: (a) arc melting and (b) steel strip.
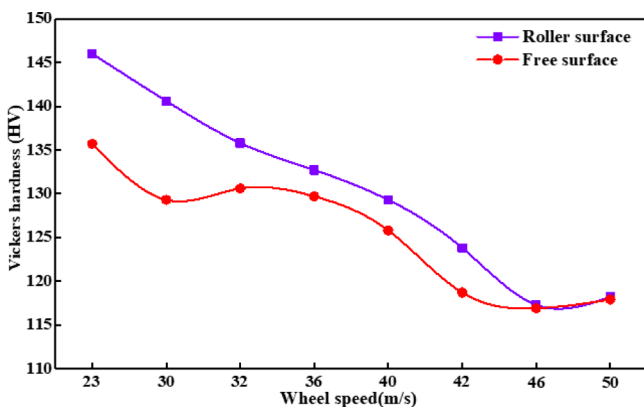

Figure 12. Vickers hardness of the Fe-6.5wt%Si steel strip with the rpm.

brittle transition in Fe-6.5wt%Si as has been identified by Herzer.[30] According to the mineral formation and transition process, the microstructure evolution, and physical property analysis, amounts of B2(FeSi) and DO_3(Fe$_3$Si) formation are the important reasons for the plasticity and workability deterioration of the Fe-6.5wt%Si steel strip. Deep subcooling solidification technology could restrain the transformation process from disordered phase A2 to B2 and DO_3, decrease the crystal grain size, improve the structure and texture, and then improve the magnetic and mechanical properties.

4. CONCLUSIONS

The rapid cooling coupling deep supercooled solidification process could promote homogeneous nucleation formation by means of decreasing the nucleation radius under a low degree of supercooling, while the high-efficiency heat conduction also provides a suitable thermodynamics and kinetics environment for crystal growth. It also could restrain the disordered phase Fe transformation into the ordered phase B2 and DO_3 significantly, enhance the thermal stability of the material, increase the cell volume and interplanar spacing, and then

improve the plasticity and magnetic properties. The metastable second phase SiC was also observed, mainly generated close to the grain boundaries, which could also promote nucleation and grain refinement. The predominant phase of the Fe-6.5wt%Si steel strip at 42 m/s is cubic Fe as well as some hexagonal Fe$_2$Si and SiC, the microstructure shows an equiaxed ferrite crystal structure with grain sizes ranging from 5 to 10 μm, and the saturation magnetizations are 302.5 emu/g in the parallel magnetic direction and 356.6 emu/g in the vertical magnetic direction.

■ AUTHOR INFORMATION

Corresponding Authors

Di Zhang − *Hebei Key Laboratory of Material Near-net Forming Technology, School of Materials Science and Engineering, Hebei University of Science and Technology, Shijiazhuang, Hebei 050018, China;* ◉ orcid.org/0000-0001-9113-7050; Email: snowfoxzd@hebust.edu.cn

Zhongqi Dong − *Hebei College of Industry and Technology, Shijiazhuang, Hebei 050091, China;* Email: dongzhongqi@126.com

Authors

Bo Wang − *Hebei Key Laboratory of Material Near-net Forming Technology, School of Materials Science and Engineering, Hebei University of Science and Technology, Shijiazhuang, Hebei 050018, China*

Guangxun Li − *Hebei Key Laboratory of Material Near-net Forming Technology, School of Materials Science and Engineering, Hebei University of Science and Technology, Shijiazhuang, Hebei 050018, China*

Yang Wang − *Hebei College of Industry and Technology, Shijiazhuang, Hebei 050091, China*

Yingtao Su − *Hebei Key Laboratory of Material Near-net Forming Technology, School of Materials Science and Engineering, Hebei University of Science and Technology, Shijiazhuang, Hebei 050018, China*

Huilan Sun − *Hebei Key Laboratory of Material Near-net Forming Technology, School of Materials Science and Engineering, Hebei University of Science and Technology, Shijiazhuang, Hebei 050018, China*

Zhihong Guo − *Hebei Key Laboratory of Material Near-net Forming Technology, School of Materials Science and Engineering, Hebei University of Science and Technology, Shijiazhuang, Hebei 050018, China*

Complete contact information is available at:
https://pubs.acs.org/10.1021/acsomega.1c03367

Notes

The authors declare no competing financial interest.

■ REFERENCES

(1) Xu, Y. K.; Li, H.; He, B. G.; Cheng, Z. P.; Zhang, W. B. Electronic Structure and Magnetic Anisotropy of Single-Layer Rare-Earth Oxybromide. *ACS Omega* **2020**, *5*, 14194−14201.

(2) Song, H.; Lee, H.; Lee, J.; Choe, J. K.; Lee, S.; Yi, J. Y.; Park, S.; Yoo, J. W.; Kwon, M. S.; Kim, J. Reprogrammable Ferromagnetic Domains for Reconfigurable Soft Magnetic Actuators. *Nano Lett.* **2020**, *20*, 5185−5192.

(3) Zheng, Z. L.; Ye, F.; Liang, Y. F.; Ding, X. F.; Lin, J. P.; Chen, G. L. Formation of Columnar-Grained Structures in Directionally Solidified Fe-6.5wt %Si Alloy. *Intermetallics* **2011**, *19*, 165−168.

(4) Liang, Y. F.; Ye, F.; Lin, J. P.; Wang, Y. L.; Chen, G. L. Effect of Annealing Temperature on Magnetic Properties of Cold Rolled High Silicon Steel Thin Sheet. *J. Alloys Compd.* **2010**, *491*, 268−270.

(5) Wang, Z. J.; Li, Y. W.; Wang, G. D.; Liu, H. T. Effects of Boron Content on the Microstructure and Mechanical Properties of Twin-Roll Strip Casting Borated Steel Sheets. *Mater. Sci. Eng., A* **2020**, *793*, 139847.

(6) Ouyang, G.; Chen, X.; Liang, Y.; Macziewski, C.; Cui, J. Review of Fe-6. 5 wt %Si High Silicon Steel—A Promising Soft Magnetic Material for Sub-KHz Application. *J. Magn. Magn. Mater.* **2019**, *481*, 234−250.

(7) Wu, Z. Y.; Jiang, Z.; Fan, X. A.; Zhou, L. J.; Wang, W. L.; Xu, K. Facile Synthesis of Fe-6.5wt %Si/SiO2 Soft Magnetic Composites as an Efficient Soft Magnetic Composite Material at Medium and High Frequencies. *J. Alloys Compd.* **2018**, *742*, 90−98.

(8) Liang, Y.; Wang, S.; Qi, J.; Ye, F.; Lin, J. Microstructure and Properties of Cost-Effective Fe−6.5 wt % Si Ribbons Fabricated by Melt-Spinning. *Scr. Mater.* **2019**, *163*, 107−110.

(9) Garibaldi, M.; Ashcroft, I.; Simonelli, M.; Hague, R. Metallurgy of High-Silicon Steel Parts Produced Using Selective Laser Melting. *Acta Mater.* **2016**, *110*, 207−216.

(10) Fan, X. A.; Wu, Z. Y.; Li, G. Q.; Wang, J.; Xiang, Z. D.; Gan, Z. H. High Resistivity and Low Core Loss of Intergranular Insulated Fe-6.5 wt %Si/SiO2 Composite Compacts. *Mater. Des.* **2016**, *89*, 1251−1258.

(11) Yu, H.; Ming, K.; Wu, H.; Yu, Y.; Bi, X. Ordering Suppression and Excellent Ductility in Soft-Magnetic Fe-6. 5 wt %Si Sheet by Hf Addition. *J. Alloys Compd.* **2018**, *766*, 186−193.

(12) Wen, S.; Han, C.; Zhang, B.; Liang, Y.; Ye, F.; Lin, J. Flow Behavior Characteristics and Processing Map of Fe-6.5wt %Si Alloys during Hot Compression. *Metals* **2018**, *8*, 186.

(13) Stanciu, C. D.; Marinca, T. F.; Chicinaș, I.; Isnard, O. Characterisation of the Fe-10 wt % Si Nanocrystalline Powder Obtained by Mechanical Alloying and Annealing. *J. Magn. Magn. Mater.* **2017**, *441*, 455−464.

(14) Feng, Y.; Li, Y.; Guo, J.; Li, J.; Du, T. Effect of Slab Reheating Temperature on Recrystallization Microstructure, Texture and Magnetic Properties of Nb-Containing Grain-Oriented Silicon Steel. *J. Magn. Magn. Mater.* **2017**, *439*, 135−143.

(15) Zhang, Z. W.; Wang, W. H.; Zou, Y.; Baker, I.; Chen, D.; Liang, Y. F. Control of Grain Boundary Character Distribution and Its Effects on the Deformation of Fe-6.5 wt % Si. *J. Alloys Compd.* **2015**, *639*, 40−44.

(16) Cai, G.; Li, C.; Cai, B.; Wang, Q. An Investigation on the Role of Texture Evolution and Ordered Phase Transition in Soft Magnetic Properties of Fe−6.5 wt %Si Electrical Steel. *J. Magn. Magn. Mater.* **2017**, *430*, 70−77.

(17) Li, C. S.; Yang, C. L.; Cai, G. J.; Wang, Q. W. Ordered Phases and Microhardness of Fe-6.5%Si Steel Sheet after Hot Rolling and Annealing. *Mater. Sci. Eng., A* **2016**, *650*, 84−92.

(18) Luo, Z.; Fan, X.'a.; Hu, W.; Luo, F.; Li, G.; Li, Y.; Liu, X.; Wang, J. Controllable SiO 2 Insulating Layer and Magnetic Properties for Intergranular Insulating Fe-6. 5wt %Si/SiO 2 Composites. *Adv. Powder Technol.* **2019**, *30*, 538−543.

(19) Yu, X.; Zhang, Z.; Xie, J. Effects of Rare Earth Elements Doping on Ordered Structures and Ductility Improvement of Fe−6.5 wt %Si Alloy. *Mater. Lett.* **2016**, *184*, 294−297.

(20) Liu, H. T.; Li, H. Z.; Li, H. L.; Gao, F.; Liu, G. H.; Luo, Z. H.; Zhang, F. Q.; Chen, S. L.; Cao, G. M.; Liu, Z. Y.; Wang, G. D. Effects of Rolling Temperature on Microstructure, Texture, Formability and Magnetic Properties in Strip Casting Fe-6.5 wt % Si Non-Oriented Electrical Steel. *J. Magn. Magn. Mater.* **2015**, *391*, 65−74.

(21) Liu, D.; Qin, J.; Zhang, Y.; Wang, Z.; Nie, J. Effect of Yttrium Addition on the Hot Deformation Behavior of Fe−6. 5 wt %Si Alloy. *Mater. Sci. Eng., A* **2020**, *797*, 140238.

(22) Fang, F.; Zhang, Y.; Lu, X.; Wang, Y.; Cao, G.; Yuan, G.; Xu, Y.; Wang, G.; Misra, R. D. K. Inhibitor Induced Secondary Recrystallization in Thin-Gauge Grain Oriented Silicon Steel with High Permeability. *Mater. Des.* **2016**, *105*, 398−403.

(23) Ouyang, G.; Macziewski, C. R.; Jensen, B.; Ma, T.; Choudhary, R.; Dennis, K.; Zhou, L.; Paudyal, D.; Anderson, I.; Kramer, M. J.; Cui, J. Effects of Solidification Cooling Rates on Microstructures and Physical Properties of Fe-6.5%Si Alloys. *Acta Mater.* **2021**, *205*, 116575.

(24) Ouyang, G.; Jensen, B.; Tang, W.; Schlagel, J.; Hilliard, B.; Pan, C.; Cui, B.; Dennis, K.; Jiles, D.; Monson, T.; Anderson, I.; Kramer, M. J.; Cui, J. Near Net Shape Fabrication of Anisotropic Fe-6.5%Si Soft Magnetic Materials. *Acta Mater.* **2020**, *201*, 209−216.

(25) Ouyang, G.; Jensen, B.; Macziewski, C. R.; Ma, T.; Meng, F.; Lin, Q.; Zhou, L.; Kramer, M.; Cui, J. Characterization of Ordering in Fe-6.5%Si Alloy Using X-Ray, TEM, and Magnetic TGA Methods. *Mater. Charact.* **2019**, *158*, 109973.

(26) Cai, G.; Li, Z.; Huang, Y. Investigation of {001} Texture Reservation and Grain Boundary Character Distribution of Fe−6. 9 wt %Si Magnetic Material by Warm−Cold Rolling. *Steel Res. Int.* **2019**, *90*, 1900093−1900019.

(27) Lemke, J. N.; Simonelli, M.; Garibaldi, M.; Ashcroft, I.; Hague, R.; Vedani, M.; Wildman, R.; Tuck, C. Calorimetric Study and Microstructure Analysis of the Order-Disorder Phase Transformation in Silicon Steel Built by SLM. *J. Alloys Compd.* **2017**, *722*, 293−301.

(28) Tang, W.; Ouyang, G.; Cui, B.; Wang, J.; Dennis, K. W.; Kramer, M. J.; Anderson, I. E.; Cui, J. Magnetic and Mechanical Properties of Grain-Refined Dy-Free Nd-Fe-B Sintered Magnets. *J. Magn. Magn. Mater.* **2021**, *521*, 167533.

(29) Cui, S.; Ouyang, G.; Ma, T.; Macziewski, C. R.; Levitas, V. I.; Zhou, L.; Kramer, M. J.; Cui, J. Thermodynamic and Kinetic Analysis of the Melt Spinning Process of Fe-6.5 wt % Si Alloy. *J. Alloys Compd.* **2019**, *771*, 643−648.

(30) Herzer, G. Modern Soft Magnets: Amorphous and Nanocrystalline Materials. *Acta Mater.* **2013**, *61*, 718−734.